

## A robust weakly compressible SPH method and its comparison with an incompressible SPH

Mostafa Safdari Shadloo<sup>1</sup>, Amir Zainali<sup>1</sup>, Mehmet Yildiz<sup>1,\*</sup>,<sup>†</sup> and Afzal Suleman<sup>2</sup>

<sup>1</sup>*Faculty of Engineering and Natural Sciences, Advanced Composites & Polymer Processing Laboratory, Sabanci University, Orhanli-Tuzla, 34956 Istanbul, Turkey*

<sup>2</sup>*Mechanical Engineering Department, University of Victoria, Victoria, BC, Canada*

### SUMMARY

This paper presents a comparative study for the weakly compressible (WCSPH) and incompressible (ISPH) smoothed particle hydrodynamics methods by providing numerical solutions for fluid flows over an airfoil and a square obstacle. Improved WCSPH and ISPH techniques are used to solve these two bluff body flow problems. It is shown that both approaches can handle complex geometries using the multiple boundary tangents (MBT) method, and eliminate particle clustering-induced instabilities with the implementation of a particle fracture repair procedure as well as the corrected SPH discretization scheme. WCSPH and ISPH simulation results are compared and validated with those of a finite element method (FEM). The quantitative comparisons of WCSPH, ISPH and FEM results in terms of Strouhal number for the square obstacle test case, and the pressure envelope, surface traction forces, and velocity gradients on the airfoil boundaries as well as the lift and drag values for the airfoil geometry indicate that the WCSPH method with the suggested implementation produces numerical results as accurate and reliable as those of the ISPH and FEM methods. Copyright © 2011 John Wiley & Sons, Ltd.

Received 1 September 2010; Accepted 14 June 2011

**KEY WORDS:** smoothed particle hydrodynamics (SPH); meshless method; bluff-body; airfoil flow; square obstacle problem; vortex shedding

### 1. INTRODUCTION

There are several complex flow phenomena such as separation, circulation and reattachment in many industrial and engineering problems. These phenomena occur in various practical applications like the heat transfer performance of fins, sudden expansion in air-conditioning ducts, flow behaviours in a diffuser, and flow around structures. Flows around a square obstacle and an airfoil are two of the widely used benchmark problems that are appropriate for understanding the aerodynamics and the fundamental characteristics of fluid flows around structures. They are relatively well documented and understood both experimentally and numerically [1–3] and therefore have become benchmark problems to validate new computational fluid dynamic approaches as well as to show the capability and the accuracy of developing in-house codes and new algorithms.

Smoothed particle hydrodynamics (SPH) is one of the most successful meshless computational methods, which was introduced separately by Gingold and Monaghan [4] and Lucy [5] in 1977 to simulate astrophysical problems. More recently, it has attracted significant attention in the fluid and solid mechanics fields as well as computer graphics communities, and in turn has been utilized to solve a wide variety of complex and highly nonlinear engineering problems including fluid–structure interactions [6], solidification [7], non-Newtonian fluid flow [8], multiphase flow [9, 10], and heat

\*Correspondence to: Mehmet Yildiz, Faculty of Engineering and Natural Sciences, Sabanci University, 34956 Tuzla, Istanbul, Turkey.

<sup>†</sup>E-mail: meyhildiz@sabanciuniv.edu

transfer problems [11], among others. In this method, rather than using an Eulerian fixed mesh, the computational domain is represented by a set of particles that are allowed to move in accordance with the solutions of relevant governing and constitutive equations. In fact, here, the term particle merely refers to a movable point that is bestowed with relevant physical and hydrodynamic transport properties such as temperature, density, viscosity and so forth. The Lagrangian nature of SPH lends itself remarkably to the simulation of a variety of complex fluid flow processes such as flow around bluff-bodies.

In the SPH literature, there are two commonly utilized approaches for solving the balance of the linear momentum equations; namely the Incompressible SPH (ISPH), and the Weakly Compressible SPH (WCSPH) methods.

The ISPH technique is based on the projection method originally proposed in [12, 13] and first implemented to the SPH method in the work of Cummins and Rudman [14], which is referred to as the standard projection method in this work. In this method, the pressure term in the momentum balance equation is computed by solving a pressure Poisson's equation. The standard projection method has been reported to suffer from the density error accumulation during the computation of the intermediate density field [15, 16]. To circumvent this and the associated problems, and consequently enhance the accuracy and the performance of the standard ISPH scheme, several modifications have been proposed for it in literature. For example, Shao and Lo [15] enforced the incompressibility in a somewhat similar manner to the one proposed in [14] with two main differences: first, they computed the intermediate velocity and then advected SPH particles; and second, they utilized the density variation as a source term rather than the divergence of the intermediate velocity. Their projection scheme has been referred to as the density invariance algorithm in the SPH literature.

Hu and Adams [17] have pointed out the density invariant ISPH algorithm leads to large density variations, thereby producing less accurate pressure field. In what follows, they have proposed the concurrent usage of the standard and the density invariant ISPH algorithms. However, such an approach requires that the pressure Poisson's equation be solved two times in each time step of a simulation, hence bringing about additional computational load to the simulation.

Recently, another novel technique referred to as particle shifting in [18–20] or artificial particle displacement in [21] has been employed to circumvent the particle clustering and associated accumulation of errors in density and pressure fields. The artificial particle displacement scheme significantly improves particle distributions in the modelling domain and thus the accuracy of the all the computed fields without causing any further computational cost. Here, it should be noted that this method is not limited to the ISPH algorithm, and also applicable to the WCSPH method.

As for the WCSPH method, the pressure is computed explicitly from a simple thermodynamic equation of state, and two commonly used forms of the equation of state can be formulated as  $p - p_o = c^2(\rho - \rho_o)$  and  $p = (c^2\rho_o/\gamma)((\rho/\rho_o)^\gamma - 1)$  where  $\rho_o$ ,  $p_o$ ,  $\gamma$  and  $c$  are the reference density (taken as the real fluid density), reference pressure, a constant and the speed of sound, respectively [14, 22]. The above introduced state equations enforce the incompressibility condition on the flow such that a small variation in density produces a relatively large change in pressure thereby limiting the dilatation of the fluid to 1%. To keep the relative incompressibility or the density variation factor, defined as  $\delta = |\rho/\rho_o - 1|$ , under 1%, the sound speed is as a rule of thumb chosen to be at least one order of magnitude larger than the maximum bulk fluid velocity  $v_{\max}$  thus resulting in a very small Mach number  $M = v_{\max}/c = \delta^{0.5} = 0.1$ .

The major advantages of WCSPH over ISPH are the ease of programming and better ordered particle distributions. Mainly for these reasons, the WCSPH method has become the most widely used approach to solve the linear momentum balance equation in SPH literature. However, unlike the ISPH method, when dealing with fluid flow problems characterized by higher Reynolds number values (i.e. greater than 100), the standard WCSPH method has been reported to suffer from large density variations, and therefore it requires the usage of a much smaller Mach number than 0.1 to avoid the formation of unphysical void regions in the computational domain [23, 24]. From the numerical stability point of view, the speed of sound has a direct effect on the permissible time-step in a given simulation, and hence directly affects the total computational cost.

There are several recent works that have aimed to compare ISPH against WCSPH for free surface and bluff body problems [24–27]. Hughes and Graham [25] have recently compared the

ISPH and WCSPH approaches for free-surface water flows. They have concluded in their work that if the standard WCSPH method is used along with some special treatments such as density smoothing, the WCSPH technique can be as correct as the ISPH approach. On the other hand, Lee *et al.* [26] illustrated that the ISPH method produces more accurate pressure fields with respect to the WCSPH through simulating three-dimensional (3D) water collapse in waterworks, and consequently concluded that the ISPH method is much more reliable in modelling free surface flow problems.

Referring back to the reported SPH simulation results in literature, one may argue that there is still no consensus in the SPH community on WCSPH being as accurate as the ISPH method. Therefore, the necessity of further comparisons of both methodologies to enforce the incompressibility condition is obvious, which is also acknowledged in [28]. To shed further light on the current understanding of the performance of both methodologies, an improved SPH algorithm for both WCSPH and ISPH approaches is proposed and implemented. The improved algorithm comprises the following: (i) the MBT method to treat solid boundaries with complex geometries [21]; (ii) an artificial particle displacement procedure to repair the nonuniformity and local fractures in particle distributions; and (iii) a corrective SPH discretization scheme to circumvent the particle inconsistency problem and in turn enhance the accuracy of the overall computation. Both WCSPH and ISPH methods are implemented and tested for two bluff body examples, namely the square obstacle and airfoil flow problems. Results of WCSPH and ISPH simulations are compared with each other for various test cases and are also validated against the outcomes of the FEM analyses. It is shown that the WCSPH approach can be as reliable as the ISPH if the artificial particle displacement, density smoothing, corrective SPH formulations, and proper boundary treatments are concurrently employed in the same problem. The improved WCSPH method can correctly model fluid flows at Reynolds numbers as high as ISPH can handle in the laminar flow regime without the necessity of using a Mach number much smaller than 0.1, and without suffering from the common issues related to particle clustering or fracture in the computational domain. As a final remark of the introduction, even though the artificial particle displacement improves the particle distribution and in turn enables the usage of a lower Mach number and consequently a larger time step, the ISPH method is still superior to WCSPH from the computational time point of view.

## 2. SMOOTHED PARTICLE HYDRODYNAMICS

The SPH method relies on the idea of smoothing field properties over a bounded domain through the formulation

$$f(\vec{r}_i) \cong \langle f(\vec{r}_i) \rangle \equiv \int_{\Omega} f(\vec{r}_j) W(r_{ij}, h) d^3\vec{r}_j, \quad (1)$$

which is referred to as the kernel approximation to an arbitrary function  $f(\vec{r}_i)$  (i.e. scalar, vectorial, or tensorial). In fact, this arbitrary function can be any hydrodynamic transport property such as temperature, enthalpy, density, viscosity and so forth. Here,  $W(r_{ij}, h)$  is a kernel function, the angle bracket  $\langle \rangle$  denotes the kernel approximation,  $\vec{r}_i$  is the position vector defining the center point of the kernel function,  $r_{ij}$  is the magnitude of the distance vector between the particle of interest  $i$  and its neighbouring particles  $j$ ,  $d^3\vec{r}_j$  is a differential volume element within the total bounded volume of the domain  $\Omega$ , and the length  $h$  defines the support domain of the particle of interest. The SPH technique in Equation (1) assumes that the fields of a given particle are affected only by that of other particles within a cutoff distance of the particle of interest with a smoothing radius  $\kappa h$  where  $\kappa$  is a coefficient associated with the particular kernel function.

A smoothing kernel function is a piece-wise spline that should satisfy several conditions: the normalization, the Dirac-delta function, compactness, spherical symmetry, and positive and even function properties. A thorough discussion on the details of these attributes of the kernel function can be found in [29] and the references therein. In SPH literature, it is possible to find different forms of piecewise smoothing kernel functions possessing the above-listed properties such as Gaussian,

cubic or quintic kernel functions. Throughout the present simulations, the compactly supported two-dimensional quintic spline kernel [22]

$$W(r_{ij}, h) = \frac{7}{478\pi h^2} \begin{cases} (3 - s_{ij})^5 - 6(2 - s_{ij})^5 + 15(1 - s_{ij})^5 & \text{if } 0 \leq s_{ij} < 1 \\ (3 - s_{ij})^5 - 6(2 - s_{ij})^5 & \text{if } 1 \leq s_{ij} < 2 \\ (3 - s_{ij})^5 & \text{if } 2 \leq s_{ij} \leq 3 \\ 0 & \text{if } s_{ij} \geq 3 \end{cases}, \quad (2)$$

is used, where  $s_{ij} = r_{ij}/h$ .

The SPH approximation for the gradient of a continuous arbitrary function can be obtained as

$$\frac{\partial f(\vec{r}_i)}{\partial x_i^k} = \sum_j \frac{m_j}{\rho_j} f(\vec{r}_j) \frac{\partial W(r_{ij}, h)}{\partial x_i^k}, \quad (3)$$

through the substitution  $f(\vec{r}_j) \rightarrow \partial f(\vec{r}_j)/\partial x_j^k$  in Equation (1), and then making use of integration by parts together with the compactness property of the kernel function as well as noting that  $\partial W(r_{ij}, h)/\partial x_i^k = -\partial W(r_{ij}, h)/\partial x_j^k$ , where the integration is replaced by the SPH summation over particle 'j' and the infinitesimal differential volume element  $d^3\vec{r}_j$  is approximated as  $d^3\vec{r}_j = m_j/\rho_j$ .

An alternative and more accurate SPH approximation for the gradient of a vector-valued function in the form of the SPH interpolation can be introduced as

$$\frac{\partial f^p(\vec{r}_i)}{\partial x_i^k} a_{ij}^{ks} = \sum_j \frac{m_j}{\rho_j} (f^p(\vec{r}_j) - f^p(\vec{r}_i)) \frac{\partial W(r_{ij}, h)}{\partial x_i^s}, \quad (4)$$

where  $a_{ij}^{ks} = \sum_j (m_j/\rho_j) r_{ji}^k (\partial W(r_{ij}, h)/\partial x_i^s)$  is a corrective second-rank tensor. This form is referred to as the corrective SPH gradient formulation that can be used to eliminate particle inconsistencies [30,31]. It should be noted that the corrective term  $a_{ij}^{ks}$  is ideally equal to Kronecker delta  $\delta^{ks}$  for a continuous function.

Two main forms of the corrective SPH approximation for the Laplacian of a vector-valued function can be written following [21] and relevant references therein as

$$\frac{\partial^2 f^p(\vec{r}_i)}{\partial x_i^k \partial x_i^k} a_{ij}^{pm} = 8 \sum_j \frac{m_j}{\rho_j} (f^p(\vec{r}_i) - f^p(\vec{r}_j)) \frac{r_{ij}^p}{r_{ij}^2} \frac{\partial W(r_{ij}, h)}{\partial x_i^m}, \quad (5)$$

$$\frac{\partial^2 f^p(\vec{r}_i)}{\partial x_i^k \partial x_i^k} (2 + a_{ij}^{ll}) = 8 \sum_j \frac{m_j}{\rho_j} (f^p(\vec{r}_i) - f^p(\vec{r}_j)) \frac{r_{ij}^s}{r_{ij}^2} \frac{\partial W(r_{ij}, h)}{\partial x_i^s}. \quad (6)$$

Throughout this work, Equation (5) is used for the Laplacian of the velocity, while Equation (6) is used for the Laplacian of pressure in the pressure Poisson's equation.

### 3. GOVERNING EQUATIONS

In this work, a transient, laminar, incompressible, viscous and Newtonian fluid flow over bluff-bodies is considered. Equations governing fluid problems in hand are the conservation of mass and linear momentum, which are expressed in the Lagrangian form and given in direct notation as

$$D\rho/Dt = -\rho \nabla \cdot \vec{v}, \quad (7)$$

$$\rho D\vec{v}/Dt = \nabla \cdot \underline{\underline{\sigma}} + \rho \vec{f}^B. \quad (8)$$

where  $\rho$  is the fluid density,  $\vec{v}$  is the divergence-free fluid velocity,  $\underline{\underline{\sigma}}$  is the total stress tensor, and  $\vec{f}^B$  is the body force term. The total stress is defined as  $\underline{\underline{\sigma}} = -p\underline{\underline{I}} + \underline{\underline{T}}$  where  $p$  is the absolute pressure,

$\underline{\underline{\mathbf{I}}}$  is the identity tensor,  $\underline{\underline{\mathbf{T}}} = \mu (\nabla \vec{\mathbf{v}} + (\nabla \vec{\mathbf{v}})^T)$  is the viscous part of the total stress tensor where  $\mu$  is the dynamic viscosity. Finally,  $D/Dt$  is the material time derivative operator.

#### 4. SMOOTHED PARTICLE HYDRODYNAMICS SOLUTION ALGORITHMS

##### 4.1. Weakly compressible smoothed particle hydrodynamics

The artificial equation of state used in the WCSPH approach presented in this work has the following form:

$$p - p_o = c^2 (\rho - \rho_o). \quad (9)$$

The speed of sound for each particle must be chosen carefully to ensure that the fluid is very closely incompressible. In addition to the commonly utilized rule of thumb as briefly discussed in the introduction section for predicting the sound speed, other dominant modelling parameters should also be considered in the estimation of the speed of sound. One such relation proposed in [22] has the following form:

$$c^2 \approx \varphi \max \left( \frac{v_{\max}^2}{\delta}, \frac{\mu}{\rho_o} \left( \frac{v_{\max}}{L_o \delta} \right), \frac{F^B L_o}{\delta} \right), \quad (10)$$

where  $\varphi$  is a problem-dependent coefficient,  $v_{\max}$  is the maximum value of the fluid velocity,  $L_o$  is a characteristic length,  $F^B$  is the magnitude of the body force, and  $\delta$  is the relative incompressibility or the density variation factor. The speed of sound chosen has a direct effect on the permissible time-step in a given simulation. The algorithm stability is controlled by the CFL condition, where the recommended time-step [32] is  $\Delta t \leq C_{\text{CFL}} h / (c + v_{\max})$  with  $C_{\text{CFL}}$  being a constant satisfying the condition  $0 < C_{\text{CFL}} \leq 1$  (in this work,  $C_{\text{CFL}} = 0.125$ ).

A predictor corrector method is used to increment the time-steps in the WCSPH algorithm. This technique is an explicit time integration scheme, and is practically simple to implement. Particle positions, densities, and velocities are computed respectively as

$$D\vec{\mathbf{r}}_i/Dt = \vec{\mathbf{v}}_i, \quad (11)$$

$$D\rho_i/Dt = k_i, \quad (12)$$

$$D\vec{\mathbf{v}}_i/Dt = \vec{\mathbf{f}}_i. \quad (13)$$

Here,  $k_i$  and  $\vec{\mathbf{f}}_i$  are the right hand sides of the conservation of mass and linear momentum equations, respectively. The time integration scheme starts with the predictor step to compute the intermediate particle positions and densities as  $\vec{\mathbf{r}}_i^{(n+1/2)} = \vec{\mathbf{r}}_i^{(n)} + 0.5\vec{\mathbf{v}}_i^{(n)} \Delta t$  and  $\rho_i^{(n+1/2)} = \rho_i^{(n)} + 0.5k_i^{(n)} \Delta t$  respectively. Having computed the intermediate particle positions and densities during the first half time step, the pressure is computed using Equation (9), while the velocity is computed by  $\vec{\mathbf{v}}_i^{(n+1)} = \vec{\mathbf{v}}_i^{(n)} + \vec{\mathbf{f}}_i^{(n+1/2)} \Delta t$ . In the next half time (the corrector step), the particle positions and densities are updated as  $\vec{\mathbf{r}}_i^{(n+1)} = \vec{\mathbf{r}}_i^{(n+1/2)} + 0.5\vec{\mathbf{v}}_i^{(n+1)} \Delta t$ , and  $\rho_i^{(n+1)} = \rho_i^{(n+1/2)} + 0.5k_i^{(n+1)} \Delta t$ . Note that to differentiate between spatial and temporal indices, the time index  $n$  is placed within brackets.

##### 4.2. Incompressible smoothed particle hydrodynamics

The ISPH approach utilized in this work is based on the standard projection method [14], which uses the principle of Hodge decomposition whereby any vector field can be broken into a divergence-free part plus the gradient of an appropriate scalar potential. Hodge decomposition can be written for a velocity field as

$$\vec{\mathbf{v}}^* = \vec{\mathbf{v}} + (\Delta t / \rho) \nabla p, \quad (14)$$



where  $\vec{v}$  is the divergence-free part of the velocity field, and  $\vec{v}^*$  is the intermediate velocity, which can be computed by solving the momentum balance equation in Equation (8) without the pressure gradient. The correct or incompressible velocity field  $\vec{v}$  can be calculated from Equation (14) with the knowledge of the pressure gradient that can be computed after the solution of a pressure Poisson's equation. The pressure Poisson's equation is formulated by taking the divergence of Equation (14) as  $\nabla \cdot \vec{v}^* / \Delta t = \nabla \cdot (\nabla p / \rho)$ , which is subjected to a Neumann boundary condition  $(\rho / \Delta t) (\vec{v}^* - \vec{v}) \cdot \vec{n} = \nabla p \cdot \vec{n}$  where  $\vec{n}$  is the unit normal vector. In the projection method, it is a common practice to replace  $\vec{v}^*$  with  $\vec{v}^{(n+1)}$  to enforce the boundary conditions so that the Neumann boundary condition reduces to  $\nabla p \cdot \vec{n} = 0$ . For a stable solution, the time step is selected in accordance with  $\Delta t \leq C_{\text{CFL}} h / v_{\text{max}}$  where  $C_{\text{CFL}} = 0.125$  in this work.

For the time integration in the ISPH approach, a first-order Euler time step scheme is used. The algorithm starts with the predictor step where the intermediate positions  $\vec{r}_i^*$  for all particles are calculated through the knowledge of preceding particle positions  $\vec{r}_i^{(n)}$  and the previous correct velocity field  $\vec{v}_i^{(n)}$  as  $\vec{r}_i^* = \vec{r}_i^{(n)} + \vec{v}_i^{(n)} \Delta t$ . The intermediate velocity field  $\vec{v}_i^*$  is calculated on the intermediate particle locations by solving the momentum balance equations with forward time integration without the pressure gradient term as  $\vec{v}_i^* = \vec{v}_i^{(n)} + \vec{f}_i^{(n)} \Delta t$ . The pressure Poisson's equation is solved using a direct solver based on the Gauss elimination method to obtain the pressure  $p_i^{(n+1)}$ , which is required to enforce the incompressibility condition. The actual velocity field  $\vec{v}_i^{(n+1)}$  can be obtained from Equation (14) by using the computed pressure  $p_i^{(n+1)}$ . Finally, with the correct velocity field for time-step  $n + 1$ , all fluid particles are moved to their new positions  $\vec{r}_i^{(n+1)} = \vec{r}_i^{(n)} + 0.5 (\vec{v}_i^{(n)} + \vec{v}_i^{(n+1)}) \Delta t$ . A more detailed implementation of the ISPH algorithm on both benchmark problems can be found in our early work [21].

#### 4.3. Artificial particle displacement

The homogeneity of the particle distribution is quite important for the accuracy and the robustness of SPH models. Highly irregular particle distributions that may occur as the solution progresses may cause numerical algorithms to break down. For instance, if the pressure field is computed correctly thereby imposing the incompressibility condition as accurately as possible, the particle motion closely follows the trajectory of the streamline, hence resulting in a linear clustering and concomitant fracture in particle distribution. In these regions, because of the lack of a sufficient number of particles, or inhomogeneous particle distribution, the gradients of field variables cannot be computed reliably. Such a situation leads to spurious fields, especially erroneous pressure values in the ISPH approach. As the computation progresses, the error in computed field variables accumulates resulting in a blow-up of the simulation. To prevent the particle clustering, the trajectory of particles can be disturbed by adding relatively small artificial displacement  $\delta r_i^k$  defined as

$$\delta r_i^k = \beta \sum_j \frac{r_{ij}^k}{r_{ij}^3} r_o^2 v_{\text{max}} \Delta t, \quad (15)$$

where  $\delta r_i^k$  is an artificial particle displacement vector,  $\beta$  is a problem-dependent parameter,  $r_o = \sum_j r_{ij} / N$  is the cutoff distance, and  $v_{\text{max}}$  is the largest particle velocity in the system. Here,  $N$  is the number of neighbors for particle  $i$  in its support domain. It is noted that for all of the simulations in this work, the problem-dependent parameter or the artificial particle displacement coefficient is kept constant and equal to 0.01 for both SPH methods. It is also noted that this coefficient should be selected carefully such that it should be small enough not to affect the physics of the flow, but also large enough to prevent the occurrence of particle clustering and fractures.

Given that  $r_{ij}^k / r_{ij}^3$  is an odd function with vanishing integral, one can write  $\sum_j r_{ij}^k / r_{ij}^3 = 0$  for a spherically symmetric particle distribution. However, if the particle distribution is asymmetric and clustered, the term  $\sum_j r_{ij}^k / r_{ij}^3 \neq 0$  is no longer equal to zero thereby implying the region with

clustered particle distribution. The artificial particle displacement is only influential in the clustered region and negligibly small in the rest of the computational domain because of  $\sum_j r_{ij}^k / r_{ij}^3 \cong 0$  provided that the particle distribution is closely uniform.

#### 4.4. Domain definition and boundary conditions

To be able to test the effectiveness of the improved SPH algorithm for both WCSPH and ISPH approaches (involving the utility of the MBT method together with the artificial particle displacement and the corrective SPH discretization scheme) for modelling fluid flow over complex geometries, we solved two benchmark flow problems, namely, two-dimensional simulations of a flow around a square obstacle and a NACA airfoil. Mass and linear momentum balance equations are solved for both test cases on a rectangular domain with the length and height of  $L = 15$  m, and  $H = 6$  m, respectively.

A square obstacle with a side dimension of 0.7 m is positioned within the computational domain with its center coordinates at  $x = L/3$  and  $y = H/2$ . Initially, a  $349 \times 145$  array (in  $x$ -direction and  $y$ -direction, respectively) of particles is created in the rectangular domain, and then particles within the square obstacle are removed from the particle array. The boundary particles are created and then distributed on solid boundaries such that their particle spacing is almost the same as the initial particle spacing of the fluid particles.

The simulation parameters, fluid density, dynamic viscosity and body force in  $x$ -direction are respectively taken as  $\rho = 1000$  kg/m<sup>3</sup>,  $\mu = 1$  kg/ms, and  $F^B = 3.0 \times 10^{-3}$  N/kg. The mass of each particle is set equal and found through the relation  $m_i = \rho_i / \max(n_i)$  where  $n_i = \sum_j W(r_{ij}, h)$  is the **number density of the particle i**. The smoothing length for all particles is equal to 1.6 times the initial particle spacing.

Boundary conditions for inlet and outlet particles are implemented such that particles crossing the outflow boundary are reinserted into the flow domain at the inlet from the same  $y$ -coordinate positions with the velocity of the inlet fluid region with its coordinates of  $x = 0$ , and  $y = 3$  so that the inlet velocity profile is not poisoned by the outlet velocity profile. The no-slip boundary condition is implemented for the square obstacle. For upper and lower walls bounding the simulation domain, the symmetry boundary condition for the velocity is applied such that  $v^y = 0$ , and  $\partial v^x / \partial y = 0$ , which is discretized by means of Equation (4). The pressure, no-slip and symmetry boundary conditions of relevant fields are implemented on both benchmark problems using the MBT method, which has been explained in detail in [21,33].

The channel geometry and the boundary conditions for the second benchmark problem are identical to the first one with the exception that the square obstacle is replaced by the NACA airfoil with a chord length of 2 m, which is created by

$$\begin{aligned} y_c &= m(2px_c - x_c^2) / p^2 & \left\{ 0 \leq x_c \leq p \right. \\ y_c &= m(2p(x_c - 1) + 1 - x_c^2) / (1 - p^2) & \left. \left\{ p < x_c \leq 1 \right. \right. \end{aligned} \quad (16)$$

where  $x_c$  and  $y_c$  are the mean camber line coordinates,  $m$  is the maximum camber in percentage of the chord, which is taken to be 5%, and  $p$  is the position of the maximum camber in percentage of the chord that is set to be 50%. The thickness distribution above and below the mean camber line is calculated as

$$y_t = 5t(0.2969x_c^{0.5} - 0.126x_c - 0.3516x_c^2 + 0.284x_c^3 - 0.1015x_c^4). \quad (17)$$

Here,  $t$  is the maximum thickness of the airfoil in percentage of chord, which is 15%. The final coordinates of the airfoil for the upper surface ( $x_U, y_U$ ) and the lower surface ( $x_L, y_L$ ) are determined using the following relations:  $x_U = x_c - y_t \sin \phi$ ,  $y_U = y_c + y_t \cos \phi$ ,  $x_L = x_c + y_t \sin \phi$ ,  $y_L = y_c - y_t \cos \phi$ , and  $\phi = \arctan(dy_c/dx)$ . Because the leading edge of the airfoil has a curve with a steeper slope, the chord is split into two parts to be able to locate more boundary particles towards the leading edge. Discrete points on the chord are created with the formula  $x_c = [(i - 1) / ilen]^n \times idis$  where  $i$  is a nodal index,  $ilen$  is the number of nodes along the chord,  $idis$  is the length of the chord, and  $n$  is the geometrical progression coefficient that controls the distance

between points on the chord. Given the chord length of 1, six inequidistant nodal points created through the geometrical progression coefficient of 2 are located along 5% of the chord length starting from the leading edge. The remaining section of the chord has 50 equidistant nodal points. The leading edge of the airfoil is located at Cartesian coordinates  $(L/5, H/2)$ .

Having obtained all coordinates of the airfoil geometry, the upper and lower surface lines are curve fitted using the least squares method of order six. In so doing, it becomes possible to compute boundary unit normals, tangents and slopes for each boundary particles. An array of  $300 \times 125$  particles in  $x$  and  $y$  directions, respectively, is created in the rectangular domain. All the initial particles falling between fitted curves for upper and lower cambers are removed from the rectangular computational domain, and then the remaining fluid particles are combined with the boundary particles to form a particle array of the computational domain. The smoothing length for all particles is set equal to 1.6 times the initial particle spacing. To show convergence, three different particle arrays, namely,  $150 \times 62$  (coarse),  $300 \times 125$  (intermediate) and  $400 \times 167$  (fine) were used. It was observed that  $300 \times 125$  array of particles is sufficient for particle number independent solutions.

## 5. RESULTS

The flows around the airfoil and square obstacle placed inside the channel were modelled for a range of Reynolds numbers  $Re = \rho l_c v_b / \mu$  where  $l_c$  is the characteristic length being set equal to the side length for the square obstacle, and the chord length for the airfoil geometry, and  $v_b$  is the bulk flow velocity. The ISPH and WCSPH modelling results are compared in terms of velocity, and pressure contours and Strouhal number for the square obstacle, and the pressure envelope, surface traction forces, and velocity gradients on the airfoil boundaries as well as the lift and drag values for the airfoil.

Figure 1 presents the modelling results as contour plots of the velocity magnitude ( $m/s$ ) for the square obstacle problem with Reynolds numbers of 100 (left) and 200 (right), respectively. One can note that the modelling outcomes of both SPH approaches are in a very good agreement with those of the FEM method. In Figure 2 are shown the pressure contours computed by ISPH, FEM

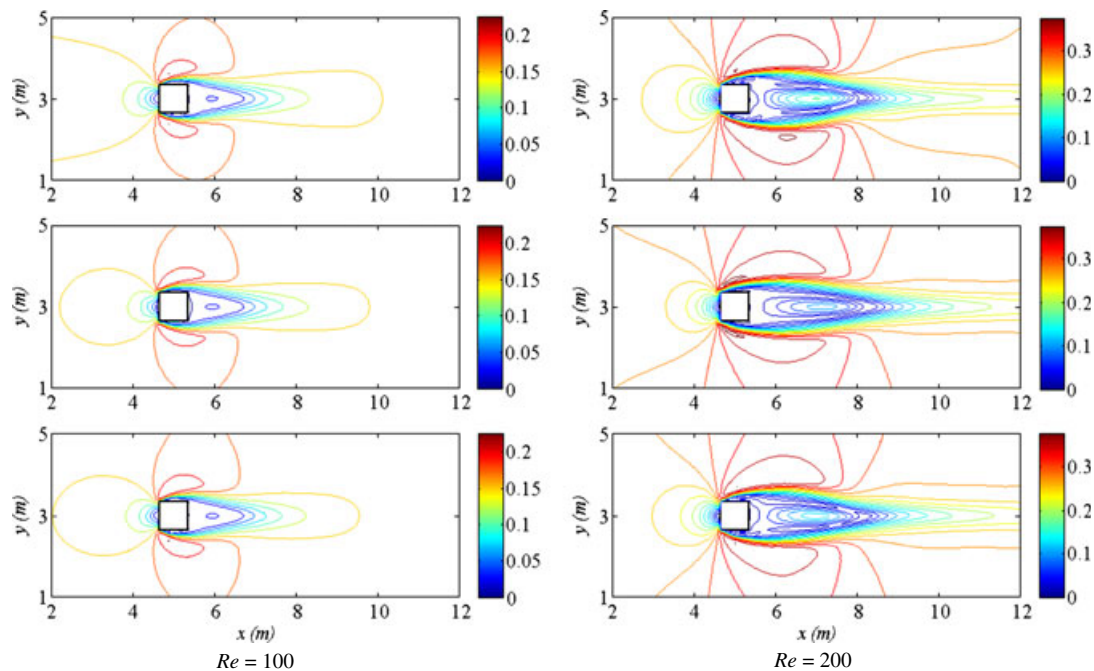


Figure 1. The comparison of ISPH (upper), FEM (middle) and WCSPH (lower) simulation results in terms of the contours of the velocity magnitude ( $m/s$ ) for  $Re = 100$  and  $Re = 200$ .



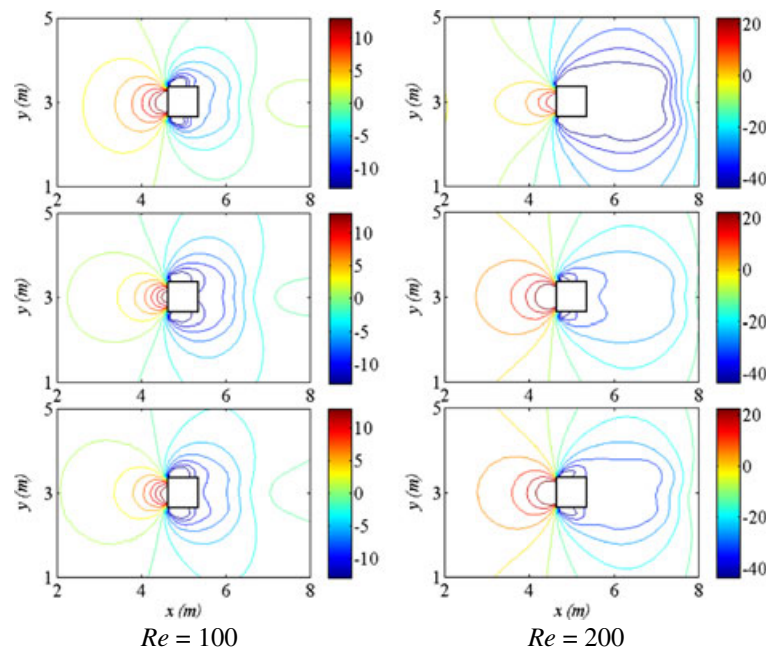


Figure 2. The comparison of ISPH (upper), FEM (middle) and WCSPH (lower) pressure contours for  $Re = 100$  and  $Re = 200$ , where pressure unit is Pascal.

and WCSPH methods for the same Reynolds numbers as in Figure 1. It is worthy to accentuate that the WCSPH pressure contours for both Reynolds numbers are as accurate as those of both ISPH and FEM and do not show any oscillatory or noisy behaviour as reported in other relevant literature [24, 34].

Early experiments and numerical studies reported the occurrence of vortex shedding at the rear edge of the square obstacle at higher Reynolds numbers [2]. In this direction, to show that both WCSPH and ISPH algorithms proposed in this work are also capable of capturing vortex shedding at the trailing edge of the square obstacle as accurately as mesh dependent solvers, simulation results of WCSPH and ISPH methods are compared with those of FEM in Figure 3 for a Reynolds number of 320 in terms of vortex shedding contours for a full period of shedding. It can be observed that the results are in a good agreement with each other with regard to the magnitude of velocities as well as the position and number of vortices.

To further comment on the correctness of the SPH modelling results presented, the Strouhal number  $St = \omega l_c / v_b$  is considered, where  $\omega$  is the frequency of vortex shedding. The computed values of the Strouhal number for WCSPH and ISPH methods for the Reynolds number of 320 are 0.139 and 0.142, respectively, which are also consistent with the experimental result reported in the literature [2].

After demonstrating the competence and success of the improved ISPH and WCSPH algorithms on a geometry with sharp corners, the proposed algorithm was also tested on a more general and complex geometry with curved boundaries and a thin body section. The sensitivity of the numerical solutions to particle numbers and the convergence of the present modelling have been recently investigated by Shadloo *et al.* [21] for the ISPH method as well as the FEM. Therefore, a comprehensive validation is not repeated here. Instead, the emphasis is placed on the validation of the numerical scheme for the WCSPH method. To do this, the velocity fields over the airfoil with the same values of the parameters were computed (Figure 4) on three different sets of particles (i.e.  $150 \times 62$  (coarse),  $300 \times 125$  (intermediate) and  $400 \times 167$  (fine)). The comparison of results on the coarse, medium and fine particle numbers clearly indicates that the intermediate particle number can produce numerical results with satisfactory accuracy given the trade-off between computational costs and capturing flow characteristics of interest. Because finer meshes are computationally expensive, the intermediate particle number is chosen for the numerical simulations presented in this article.

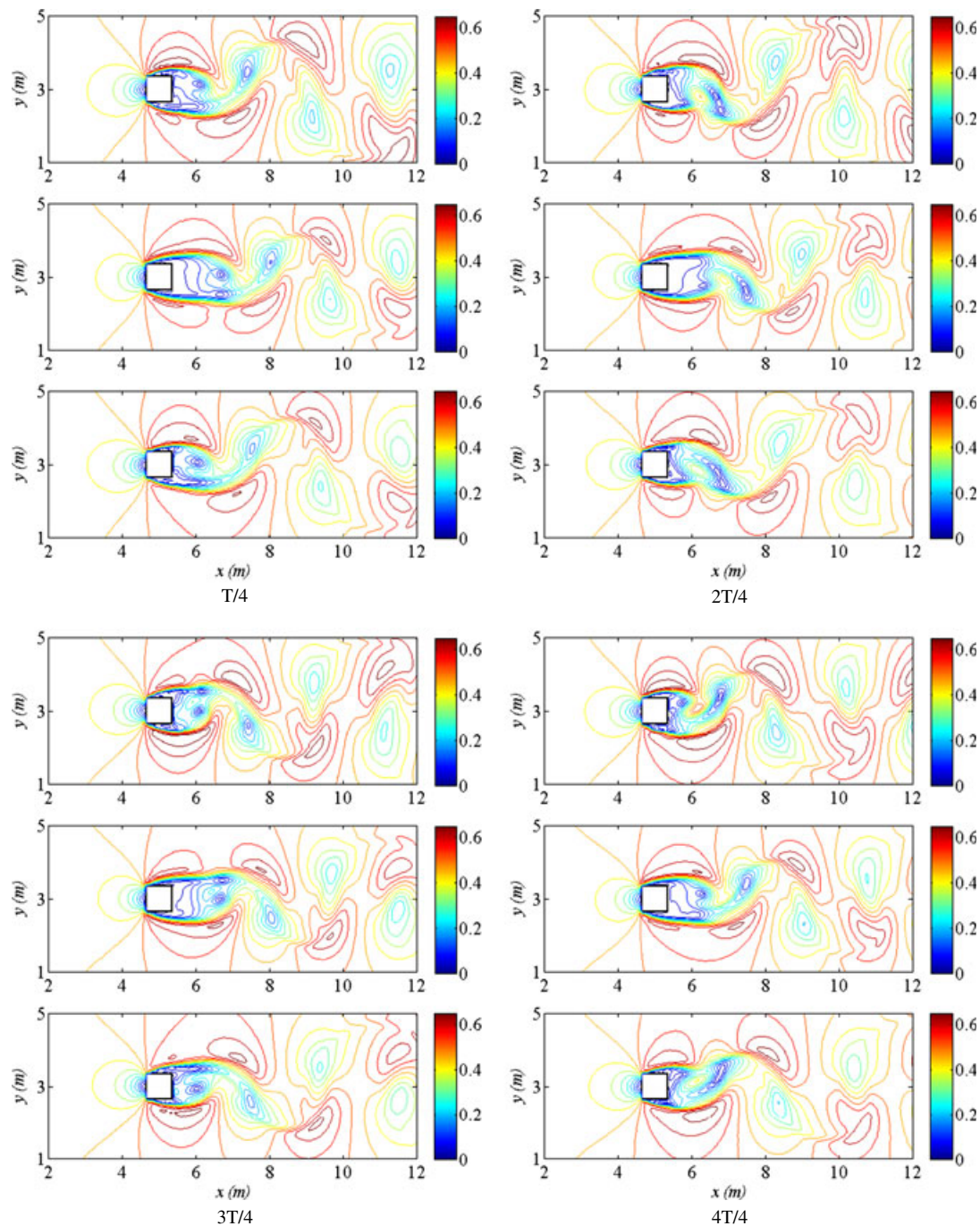


Figure 3. The comparison of a full period of vortex shedding velocity contours obtained with ISPH (upper), FEM (middle) and WCSPH (lower) for the Reynolds number of 320.

The simulations are performed on a workstation using an Intel® Core™ i7-950 Processor (8M Cache, 3.06 GHz, 4.80 GT/s) under a WINDOWS XP (64-Bit Edition) operating system. The computational cost in terms of the CPU time for the coarse, medium and fine particle numbers for one second of the real simulation time is respectively 21.2 s, 85.6 s and 159.2 s for the ISPH method, and 128.9 s, 1352.8 s and 2651.3 s for the WCSPH method.

Figures 5 and 6 compare the velocity contours of ISPH (upper), FEM (middle) and WCSPH (lower) for the angles of attack of  $5^\circ$  and  $15^\circ$  respectively (contours show the velocity magnitude,

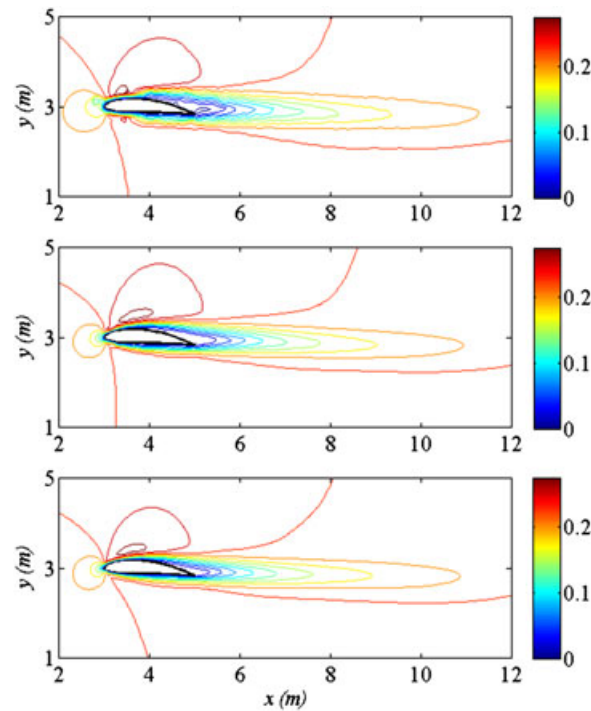


Figure 4. The velocity fields in terms of velocity magnitudes over the airfoil (with an angle of attack of  $5^\circ$  at Reynolds number of 420) computed on three different sets of particles by the WSPH method, namely  $150 \times 62$  (coarse),  $300 \times 125$  (intermediate) and  $400 \times 167$  (fine), for which results are given from top to bottom, respectively.

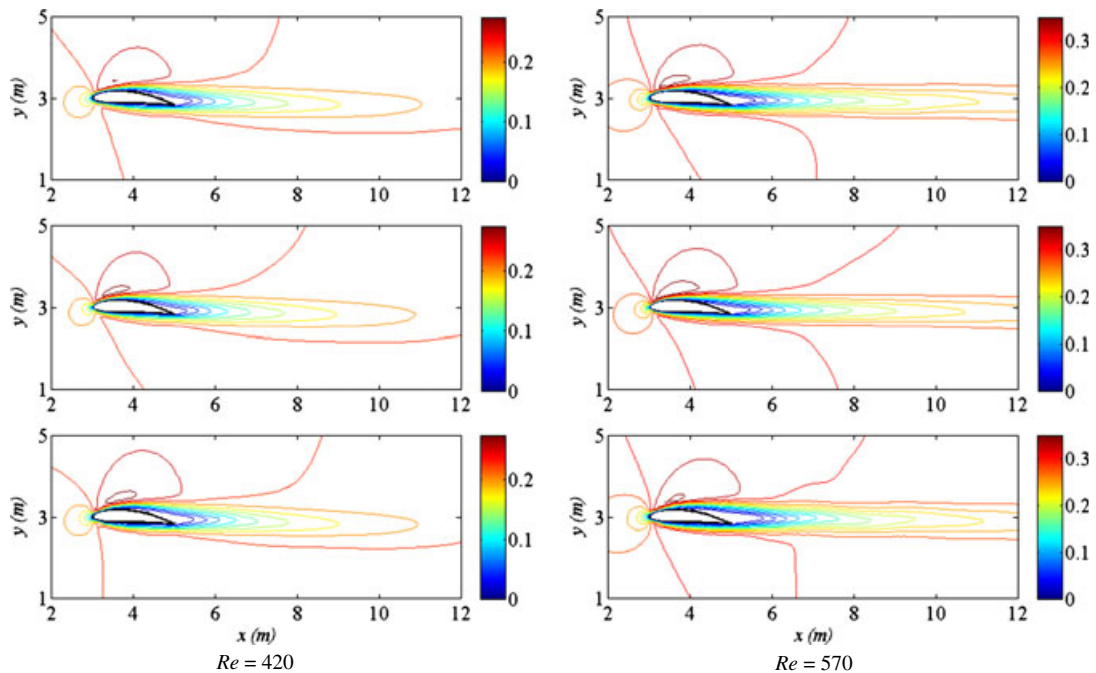


Figure 5. The comparison of ISPH (upper), FEM (middle) and WSPH (lower) velocity contours for the angle of attack of  $5^\circ$  at  $Re = 420$  and  $Re = 570$ .



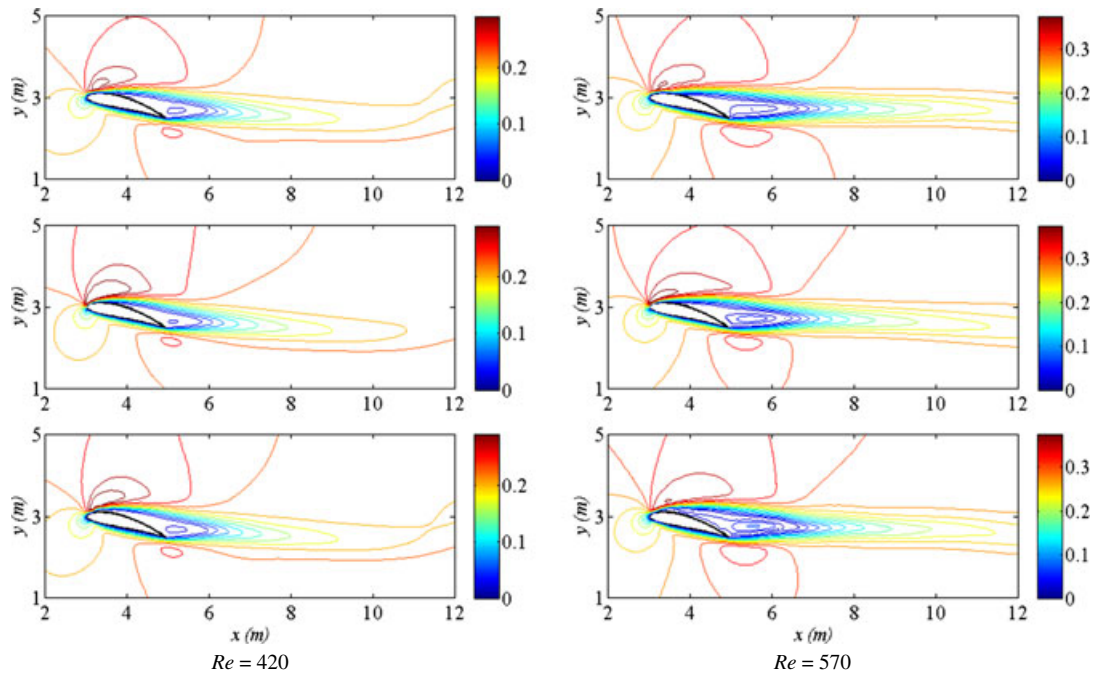


Figure 6. The comparison of ISPH (upper), FEM (middle) and WCSPH (lower) velocity contours for the angle of attack of  $15^\circ$  at  $Re = 420$  and  $Re = 570$ .

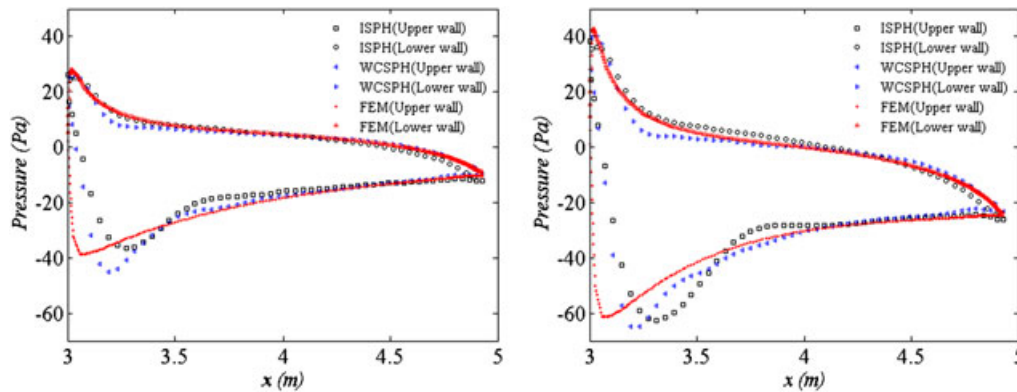


Figure 7. The comparison of pressure envelopes for the angle of attack of  $15^\circ$  at  $Re = 420$  (left) and  $Re = 570$  (right).

m/s) for the Reynolds numbers of 420 (left) and 570 (right). Similar to the previous benchmark problem, both WCSPH and ISPH results are in good agreement with those of the mesh dependent FEM technique. In all simulations, the results of WCSPH are as accurate as the ISPH ones. The figures further illustrate that the proposed algorithm is also very successful in simulating the flow around the airfoil geometry with different angles of attack across the flow field.

Figure 7 provides a comparison for the WCSPH, ISPH and FEM pressure envelopes around the airfoil for the angle of attack of  $15^\circ$  with the Reynolds numbers of 420 (left) and 570 (right). The results of both SPH approaches are consistent with those corresponding to the mesh dependent solver. It is noted that the WCSPH pressure envelop is more accurate and is in a closer agreement with the FEM method than that of ISPH, especially at the higher Reynolds number. Observing the figures, one can notice that there is a small discrepancy in pressure values compared with the FEM results for the upper camber in the vicinity of the leading edge and the stagnation point. Also, the

$x$ -coordinates of minimum pressure for both WCSPH and ISPH methods are slightly greater than that of the FEM method. These discrepancies in pressure values might be attributed to the dynamic nature of the SPH method because fluid particles are in continuous motion. This local temporary scarcity of particles near the solid boundaries might deteriorate the accuracy of the computed pressure because the SPH gradient discretization scheme is rather sensitive to the particle deficiencies within the influence domain of the smoothing kernel function.

To have an additional quantitative comparison between the proposed SPH methods and the FEM analysis, the total surface force  $\vec{F} = \underline{\underline{\sigma}} \cdot \vec{n} da$  acting on the upper and the lower cambers are plotted as a function of the chord length, as denoted in Figure 8 where  $da$  is the area of a surface element. One can notice that there exist similar discrepancies in total surface forces between SPH and FEM results as in the case of pressure values. This is due to the fact that at this Reynolds number range, the pressure force is dominant over the viscous forces. Figure 9 illustrates the components of the velocity gradient on the airfoil boundary for the upper camber. Upon integrating the  $x$ -component and  $y$ -component of the total surface force over the airfoil, one can calculate the lift and drag forces, respectively. The lift and drag forces acting on the airfoil with the angle of attack of  $15^\circ$  for the Reynolds numbers of 420 and 570 are reported in Table I. Given the difficulty of having more particles in the vicinity of the airfoil boundaries in the SPH method unlike the mesh-dependent methods because of the dynamic nature of SPH particles, satisfactorily good agreement is observed between SPH and FEM results.

Figure 10 presents the close-up view of particle positions around airfoils with the angle of attack of  $15^\circ$  and Reynolds numbers of 570 (left) and 1400 (right) for the ISPH and WCSPH methods. Incompressibility condition is enforced more accurately in the ISPH method than in the WCSPH

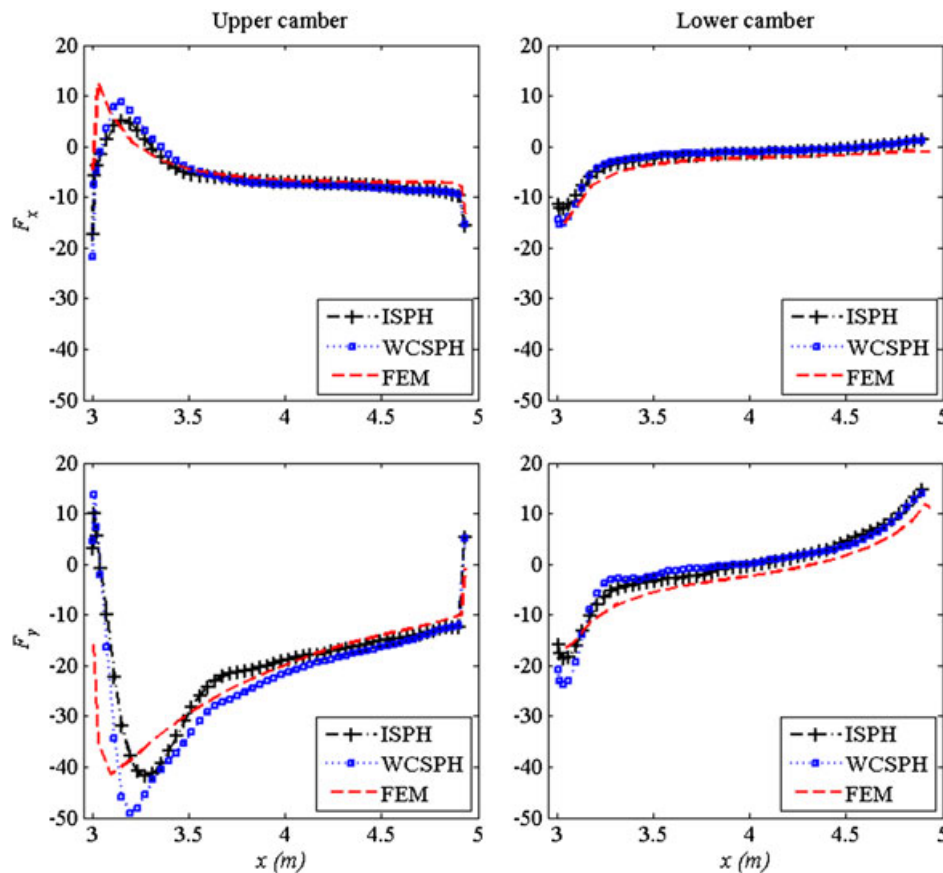


Figure 8. The comparison of total forces on the upper and lower cambers of the airfoil for the angle of attack of  $15^\circ$  at  $Re = 420$ .



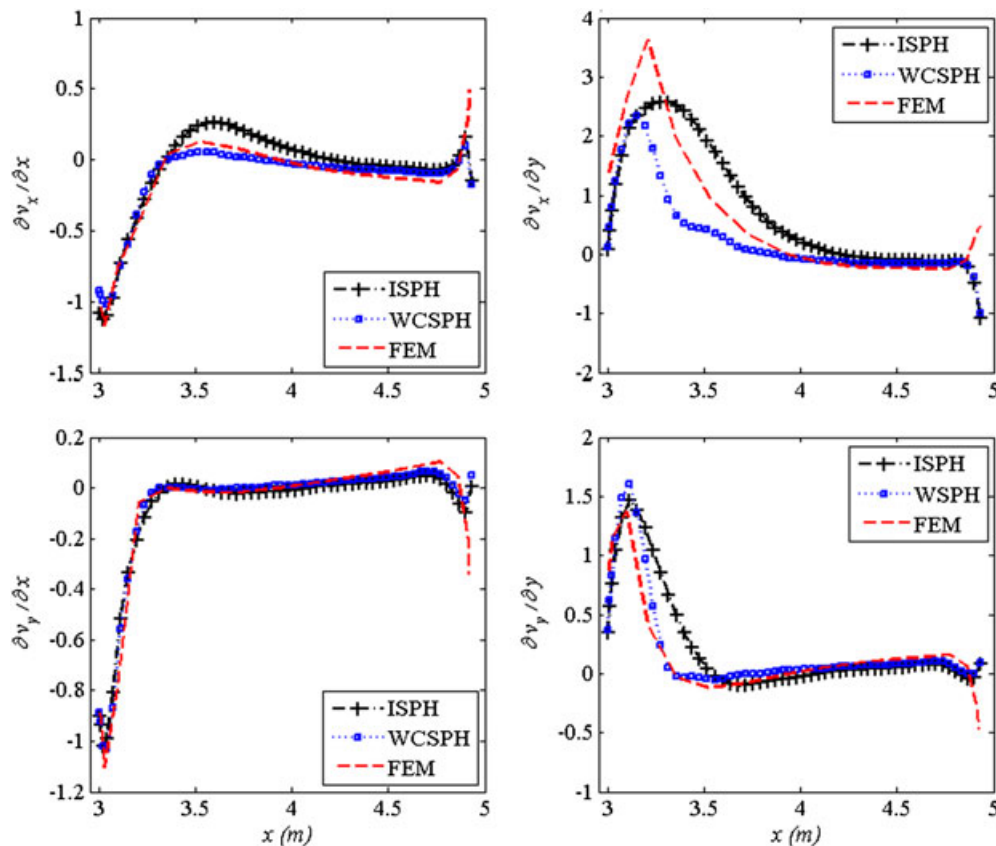


Figure 9. The comparison of the components of the velocity gradient on the upper camber of the airfoil with the angle of attack of  $15^\circ$  at  $Re = 420$ .

Table I. The lift and drag forces acting on the airfoil with the angle of attack of  $15^\circ$  at  $Re = 420$  and  $Re = 570$ .

Re	ISPH		FEM		WCSPH	
	Lift	Drag	Lift	Drag	Lift	Drag
420	43.2813	16.9709	52.0167	17.5942	49.2342	16.5904
570	66.4510	26.4433	69.9198	25.9040	62.9650	24.4302

method. Therefore, particles in the WCSPH method do not have a strong tendency to follow the streamline trajectory. As a consequence, the WCSPH technique does not suffer from particle deficiency around the upper camber as much as ISPH. These figures also illustrate the effectiveness of using the MBT method to treat difficult geometries, which might not be achievable with other boundary treatment methods proposed for meshless numerical approaches. For both the low and high Reynolds number values (i.e.  $Re = 570$ , and  $Re = 1400$ ) there are no particle deficiencies in the domains of interest for the WCSPH method.

It is noteworthy to emphasize that without the artificial particle displacement algorithm presented and implemented in this work, nonphysical particle fractures occur around the airfoil geometry because of the relatively high velocity and the tendency of SPH particles to follow a streamline trajectory as illustrated in Figure 11. This brings about erroneous density, pressure and velocity fields and in turn blows up the simulations even for relatively small Reynolds numbers (i.e.  $Re = 100 - 300$ ) and angle of attack values. In passing, it should be mentioned that within the scope of this work, the artificial stress method [35, 36] has also been considered and implemented

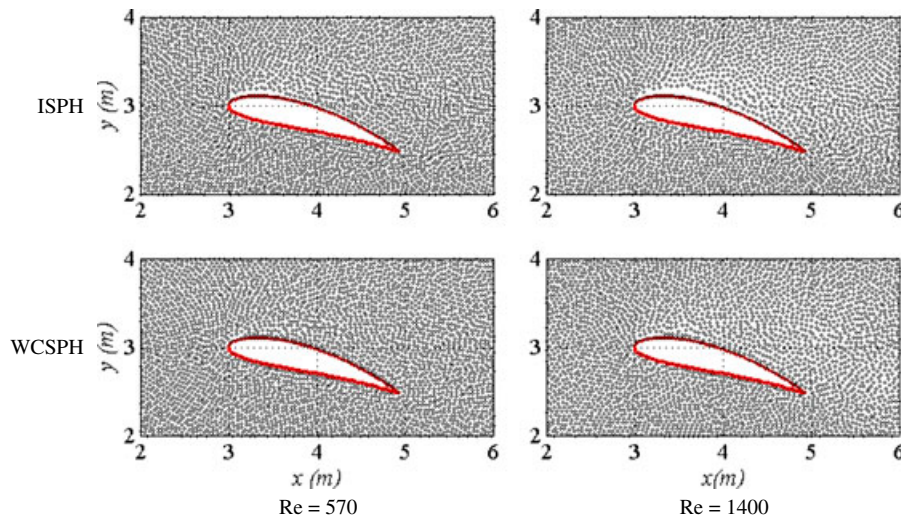


Figure 10. The close-up view of particle positions around airfoils with the angle of attack of  $15^\circ$  at  $Re = 570$  and  $Re = 1400$  for ISPH and WCSPH methods, respectively.

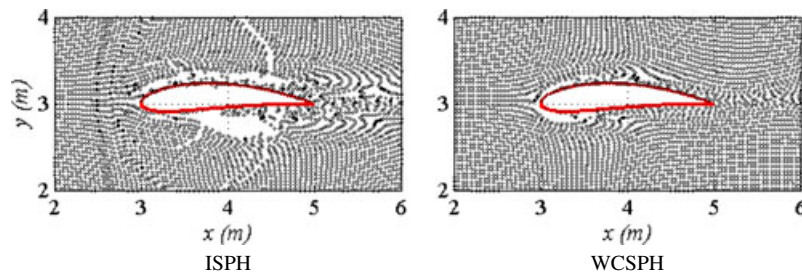


Figure 11. The close-up view of particle positions around airfoils with the angle of attack of  $5^\circ$  at  $Re = 300$  without using the artificial particle displacement method.

as a possible remedy for particle fractures for both the ISPH and the WCSPH techniques. It was observed that the artificial stress method could partially eliminate particle clustering and associated instabilities in computational domains and is effective only up to a Reynolds number of roughly 120. This may lead one to conclude that the particle disorderliness has a significant effect on the existence of numerical instabilities in the SPH method.

Another approach to avert the formation of particle clustering and fractured domains in the WCSPH method is to increase the speed of sound value. Although this treatment might be a remedy for void formations as also reported in [23,24], it increases the computational cost significantly. For example, the computational costs to achieve one second of the real simulation are 4665.7 s, 1352.8 s, 1069.8 s, and 761.2 s in terms of CPU time for large ( $M = 0.025$ ), default ( $M = 0.1$ ), small ( $M = 0.173$ ), and very small ( $M = 0.316$ ) sound speeds, respectively. The large and default speed of sound values keep the density variation less than 1%, and small and very small speed of sound values are chosen such that the density variation is less than 3% and 10% in that order. In Figure 12 are given particle distributions and the contour plots for the density field corresponding to default, small and very small speed of sound values. One can see that the artificial particle displacement permits the usage of much smaller sound speed values without the concern of any fractured regions in particle distribution. Despite the fact that small and very small sound speed values do not cause any noticeable problem in the particle distribution, they cannot enforce the incompressibility. Therefore, the sound speed value referred to as the default has been used to generate all the reported WCSPH results in this work.

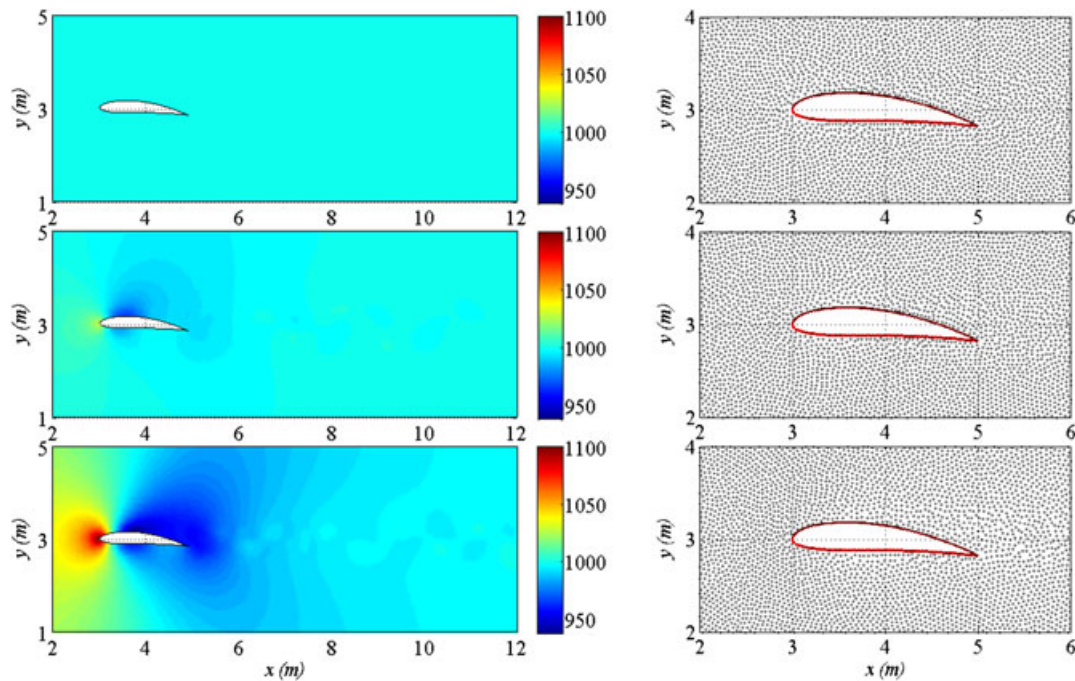


Figure 12. The density contours (left) and corresponding particle distributions (right) around the airfoils obtained with the WCSPH method with the angle of attack of  $5^\circ$  at  $Re = 1000$ .

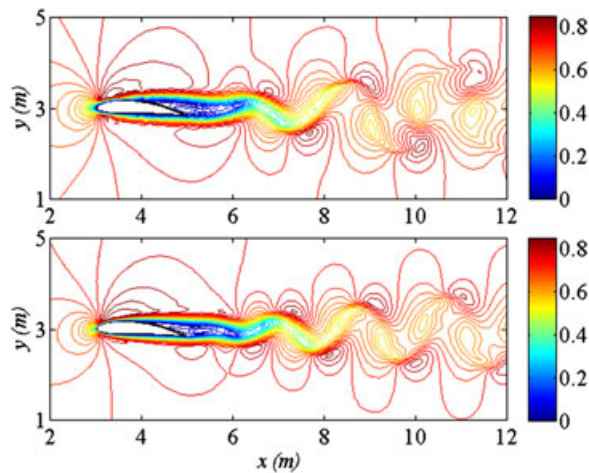


Figure 13. The comparison of vortex shedding contours produced by WCSPH (upper) and FEM (lower) methods for the angle of attack of  $5^\circ$  at  $Re = 1400$ .

Having shown that the WCSPH algorithm presented in this work can simulate fluid flow around the bluff bodies as successfully and accurately as ISPH and FEM, for the sake of completeness, it is prudent and valuable to show that it can also model laminar fluid flow over bluff bodies with high Reynolds number values. Figure 13 shows a snapshot of the vortex shedding contours produced by WCSPH (upper) and FEM (lower) methods for the angle of attack of  $5^\circ$  and the Reynolds number of 1400 (colors denote the velocity magnitude (m/s)). As in the case of the presented square obstacle results, the WCSPH result is also satisfactorily in agreement with FEM regarding the magnitude of velocities as well as the position and number of vortices for the airfoil geometry.

## 6. CONCLUSION

In this work, solutions for flow over an airfoil and square obstacle are presented to demonstrate that the WCSPH and ISPH algorithms integrated concomitantly with the MBT method, artificial particle displacement, and the corrective SPH discretization scheme can simulate flow around complex geometries accurately and reliably. The WCSPH and ISPH results were compared in terms of velocity and pressure contours and Strouhal number for the former benchmark problem, and velocity contours, the pressure envelope, surface traction forces, and velocity gradients on the airfoil boundaries as well as the lift and drag values for the latter one. Simulation results for both SPH methods were validated using the FEM method. Excellent agreements among the results were observed. It was demonstrated that the improved WCSPH method is able to capture the complex physics of bluff-body flows such as flow separation, wake formation at the trailing edge, and vortex shedding as accurately as the ISPH method without experiencing any particle clustering and fracture problems. It has been documented in the SPH open literature that the WCSPH method may not estimate pressure fields reliably and is believed to produce noisy and oscillatory pressure fields. It is further considered that if a relatively low speed of sound value is used, the WCSPH method cannot simulate flow problems with high Reynolds number values and leads to the occurrence of void regions in the computational domain. It was shown in this work that with the proper and judicious implementation of the proposed algorithms, for all Reynolds numbers in the laminar regimes, the WCSPH technique can provide stable simulations and accurate results without any noticeable noise in pressure values. Also, the Mach number equal to 0.1 satisfactorily enforces the fluid incompressibility condition with the density variation less than 1%.

## ACKNOWLEDGEMENTS

Funding provided by the European Commission Research Directorate General under Marie Curie International Reintegration Grant program with the grant agreement number of PIRG03-GA-2008-231048 is gratefully acknowledged. The first author also acknowledges the Yousef Jameel scholarship.

## REFERENCES

1. Mueller TJ, Batill SM. Experimental studies of separation on a two-dimensional airfoil at low Reynolds number. *AAIA Journal* 1982; **20**(4):456–463.
2. Okjima A. Strouhal numbers of rectangular cylinders. *Journal of Fluid Mechanics* 1982; **123**:379–398.
3. Mehta UB, La Z. Starting vortex, separation bubbles and stall: a numerical study of laminar unsteady flow around an airfoil. *Journal of Fluid Mechanics* 1975; **67**:227–256.
4. Gingold RA, Monaghan JJ. Smooth Particle Hydrodynamics: theory and application to non spherical stars. *Monthly Notices of the Royal Astronomical Society* 1977; **181**:375–389.
5. Lucy LB. A numerical approach to the testing of the fission hypothesis. *The Astronomical Journal* 1977; **82**(12):1013–1024.
6. Antoci C, Gallati M, Sibilla S. Numerical simulation of fluid–structure interaction by SPH. *Computers and Structures* 2007; **85**(11–14):879–890.
7. Monaghan JJ, Huppert HE, Worster MG. Solidification using smoothed particle hydrodynamics. *Journal of Computational Physics* 2005; **206**(2):684–705.
8. Fang J, Owens RG, Tacher L, Parriaux A. A numerical study of the SPH method for simulating transient viscoelastic free surface flows. *Journal of Non-Newtonian Fluid Mechanics* 2006; **139**(1–2):68–84.
9. Monaghan JJ, Kocharyan A. SPH simulation of multi-phase flow. *Computer Physics Communications* 1995; **87**(1–2):225–235.
10. Shadloo MS, Yildiz M. Numerical modeling of Kelvin–Helmholtz instability using smoothed particle hydrodynamics. *International Journal for Numerical Methods in Engineering* 2011. DOI: 10.1002/nme.3149.
11. Rook RA, Yildiz M, Dost S. Modelling transient heat transfer using SPH and implicit time integration. *Journal of Numerical Heat Transfer, Part B* 2007; **51**:1–23.
12. Chorin AJ. Numerical solutions of the Navier–Stokes equations. *Mathematics of Computation* 1968; **22**(104):745–762.
13. Chorin AJ. On the convergence of discrete approximations to the Navier–Stokes equations. *Mathematics of Computation* 1969; **23**(106):341–353.
14. Cummins SJ, Rudman M. An SPH projection method. *Journal of Computational Physics* 1999; **152**(2):584–607.
15. Shao S, Lo EYM. Incompressible SPH method for simulating Newtonian and non-Newtonian flows with a free surface. *Advances in Water Resources* 2003; **26**(7):787–800.



16. Pozorski J, Wawreńczuk A. Sph computation of incompressible viscous flows. *Journal of Theoretical Applied Mechanics* 2002; **40**(4):917–937.
17. Hu XY, Adams NA. An incompressible multi-phase SPH method. *Journal of Computational Physics* 2007; **227**(1):264–278.
18. Nestor R, Basa M, Quinlan N. Moving boundary problems in the finite volume particle method. *ERCOFTAC SIG SPHERIC IIIrd International workshop*, Lausanne, Switzerland, 2008; 109–114.
19. Xu R. An improved incompressible smoothed particle hydrodynamics method and its application in free-surface Simulations. *Ph.D. Thesis*, University of Manchester, U.K., 2010.
20. Xu R, Stansby P, Laurence D. Accuracy and stability in incompressible SPH (ISPH) based on the projection method and a new approach. *Journal of Computational Physics* 2009; **228**(18):6703–6725.
21. Shadloo MS, Zainali A, Sadek SH, Yildiz M. Improved incompressible smoothed particle hydrodynamics method for simulating flow around bluff bodies. *Computer Methods in Applied Mechanics and Engineering* 2011; **200**(9–12):1008–1020.
22. Morris JP, Fox PJ, Zhu Y. Modeling low Reynolds number incompressible flows using SPH. *Journal of Computational Physics* 1997; **136**(1):214–226.
23. Issa R, Lee ES, Violeau D, Laurence DR. Incompressible separated flows simulations with the smoothed particle hydrodynamics gridless method. *International Journal for Numerical Methods in Fluids* 2005; **47**(10–11):1101–1106.
24. Lee E-S, Moulinec C, Xuc R, Violeau D, Laurence D, Stansby P. Comparisons of weakly compressible and truly incompressible algorithms for the SPH mesh free particle method. *Journal of Computational Physics* 2008; **227**(18):8417–8436.
25. Hughes JP, Graham DI. Comparison of incompressible and weakly-compressible SPH models for free-surface water flows. *Journal of Hydraulic Research* 2010; **48**(Extra Issue):105–117.
26. Lee E-S, Violeau D, Issa R, Ploix S. Application of weakly compressible and truly compressible SPH to 3-D water collapse in waterworks. *Journal of Hydraulic Research* 2010; **48**(Extra Issue):50–60.
27. Khayyer A, Gotoh H. On particle-based simulation of a dam break over a wet bed. *Journal of Hydraulic Research* 2010; **48**(2):238–249.
28. Gesteira MG, Rogers BD, Violeau D, Grassa JM, Crespo AJC. Foreword: SPH for free-surface flows. *Journal of Hydraulic Research* 2010; **48**(Extra Issue):3–5.
29. Liu MB, Liu GR. Smoothed Particle Hydrodynamics (SPH): an overview and recent developments. *Archives of Computational Methods in Engineering* 2010; **17**(1):25–76.
30. Vila JP. Particle weighted methods and Smooth particle hydrodynamics. *Mathematical Models and Methods in Applied Sciences* 1999; **9**(2):161–209.
31. Bonet J, Lok TSL. Variational and momentum preservation aspects of smooth particle hydrodynamics formulations. *Computer Methods in Applied Mechanics Engineering* 1999; **180**(1–2):97–115.
32. Monaghan JJ. Smoothed particle hydrodynamics. *Reports on Progress in Physics* 2005; **68**(8):1703–1759.
33. Yildiz M, Rook RA, Suleman A. SPH with the multiple boundary tangent method. *International Journal for Numerical Methods in Engineering* 2009; **77**(10):1416–1438.
34. Delorme L, Colagrossi A, Souto-Iglesias A, Zamora-Rodriguez R, Botia-Vera E. A set of canonical problems in sloshing, Part I: Pressure field in forced roll—comparison between experimental results and SPH. *Ocean Engineering* 2009; **36**(2):168–178.
35. Monaghan JJ. SPH without a tensile instability. *Journal of Computational Physics* 2000; **159**(2):290–311.
36. Gray JP, Monaghan JJ, Swift RP. SPH elastic dynamics. *Computer Methods in Applied Mechanics and Engineering* 2001; **190**(49–50):6641–6662.